

Regioselective hydroformylation of propene catalysed by rhodium-zeolite

<https://doi.org/10.1038/s41586-024-07342-y>

Received: 25 August 2023

Accepted: 21 March 2024

Published online: 24 April 2024

 Check for updates

Xiangjie Zhang^{1,2,3,9}, Tao Yan^{1,2,3,9}, Huaming Hou^{2,9}, Junqing Yin^{4,9}, Hongliu Wan²✉, Xiaodong Sun², Qing Zhang⁵, Fanfei Sun⁶, Yao Wei⁶, Mei Dong¹, Weibin Fan¹, Jianguo Wang³, Yujie Sun⁷, Xiong Zhou⁸, Kai Wu⁸, Yong Yang^{1,2}✉, Yongwang Li^{1,2} & Zhi Cao^{1,2}✉

Hydroformylation is an industrial process for the production of aldehydes from alkenes^{1,2}. Regioselective hydroformylation of propene to high-value *n*-butanal is particularly important, owing to a wide range of bulk applications of *n*-butanal in the manufacture of various necessities in human daily life³. Supported rhodium (Rh) hydroformylation catalysts, which often excel in catalyst recyclability, ease of separation and adaptability for continuous-flow processes, have been greatly exploited⁴. Nonetheless, they usually consist of rotationally flexible and sterically unconstrained Rh hydride dicarbonyl centres, only affording limited regioselectivity to *n*-butanal^{5–8}. Here we show that proper encapsulation of Rh species comprising Rh(I)-*gem*-dicarbonyl centres within a MEL zeolite framework allows the breaking of the above model. The optimized catalyst exhibits more than 99% regioselectivity to *n*-butanal and more than 99% selectivity to aldehydes at a product formation turnover frequency (TOF) of 6,500 h^{−1}, surpassing the performance of all heterogeneous and most homogeneous catalysts developed so far. Our comprehensive studies show that the zeolite framework can act as a scaffold to steer the reaction pathway of the intermediates confined in the space between the zeolite framework and Rh centres towards the exclusive formation of *n*-butanal.

Rh-catalysed regioselective hydroformylation of propene to yield industrially important *n*-butanal represents one of the most prominent catalytic processes in the chemical industry (Fig. 1a). Supported Rh catalysts have many inherent strengths as used in this transformation. However, they have fallen short in attained regioselectivity towards the thermodynamically least stable (anti-Markovnikov) *n*-butanal. We are particularly inspired by the classical transition-state shape selectivity in zeolite catalysis, in which the shape of the pore inhibits the formation of a bulky intermediate that is too large to fit inside⁹. We propose to further extend this concept from zeolite to zeolite-confined metal sites through deliberate confinement of low-atomicity Rh species within a MEL zeolite framework (Fig. 1b). We reason that the key reaction intermediates bound to the Rh could be effectively confined into a narrower space enveloped between the zeolite framework and the Rh sites. As such, even a small difference in adopted configuration between the linear and branched intermediates, when positioned into the appropriately confined microenvironment, might result in distinct shape selectivity. We thus anticipate that highly regioselective formation of *n*-butanal from less bulky linear intermediate could be achieved.

Our Rh-zeolite catalyst was synthesized by means of a one-pot hydrothermal crystallization process¹⁰, followed by the oxidative disruption

of the imbedded Rh clusters (Fig. 2a). The purely siliceous MEL zeolites were prepared and Rh was encapsulated within their pores, as confirmed by X-ray diffraction (Supplementary Fig. 1) and annular dark-field scanning transmission electron microscopy (ADF-STEM) (Supplementary Fig. 2) studies. The Rh loading was determined as 0.17 wt% (Supplementary Table 1) and approximately 97% of the loaded Rh species were successfully positioned within the pores of MEL zeolite (Supplementary Table 2). For brevity, the as-prepared sample was termed **0.17Rh@MEL**. An oxidative disruption of the Rh clusters under elevated-pressure ambient CO, a well-known process occurring on various types of oxide support, leads to the formation of highly dispersed *gem*-dicarbonyl species [Rh(CO)₂] (refs. 11–13). We proposed that this phenomenon may also take place on the zeolite support, enabling to create molecularly well-defined Rh sites within the zeolite channels. Accordingly, we performed the oxidative disruption experiment of **0.17Rh@MEL** (see Methods for details) and designated the post-treatment material as **0.17Rh_{op}@MEL**. ADF-STEM characterization (Supplementary Figs. 3–5) revealed that the encapsulated Rh species in the **0.17Rh_{op}@MEL** existed as either subnanometre clusters (Fig. 2b,d,e) or isolated Rh atoms (Fig. 2c,f,g). Notably, highly dispersed subnanometre Rh clusters with an average size of 0.6 nm were prevalent in the sample. Also, the ADF-STEM imaging along the <100> direction

¹State Key Laboratory of Coal Conversion, Institute of Coal Chemistry, Chinese Academy of Sciences, Taiyuan, China. ²National Energy Center for Coal to Clean Fuels, Synfuels China Technology Co., Ltd., Beijing, China. ³University of Chinese Academy of Sciences, Beijing, China. ⁴Institute of Advanced Study, Chengdu University, Chengdu, China. ⁵Shanghai Key Laboratory of High-resolution Electron Microscopy, ShanghaiTech University, Shanghai, China. ⁶Shanghai Synchrotron Radiation Facility, Shanghai Advanced Research Institute, Chinese Academy of Sciences, Shanghai, China. ⁷Department of Chemistry, University of Cincinnati, Cincinnati, OH, USA. ⁸Beijing National Laboratory for Molecular Sciences, College of Chemistry and Molecular Engineering, Peking University, Beijing, China. ⁹These authors contributed equally: Xiangjie Zhang, Tao Yan, Huaming Hou, Junqing Yin. ✉e-mail: wanHongliu@synfuelschina.com.cn; yyong@sxicc.ac.cn; caozhi@sxicc.ac.cn

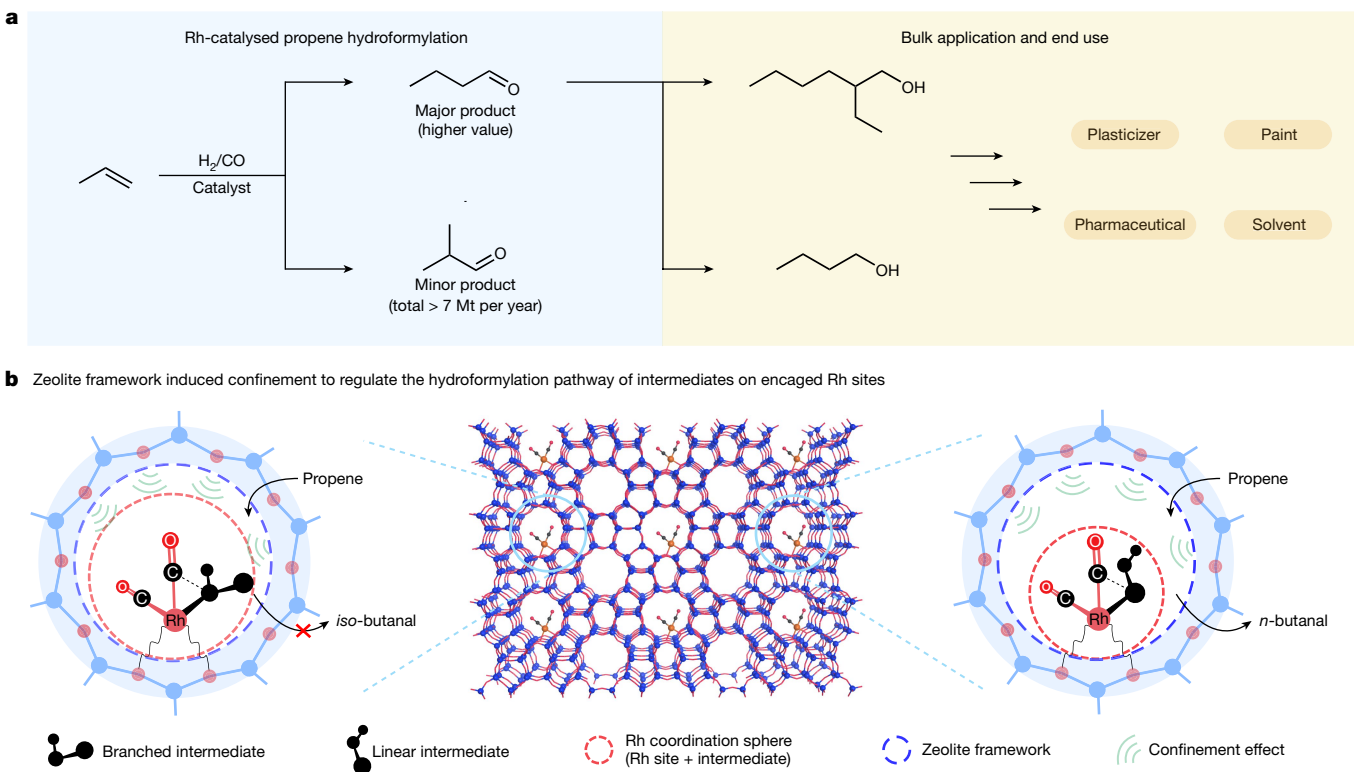


Fig. 1 | Industrial propene hydroformylation and our proposed heterogeneous Rh-zeolite system. **a**, Rh-catalysed homogeneous hydroformylation of propene in industry. **b**, Our design principle of Rh-zeolite catalysts by extending the classical transition-state shape selectivity in zeolite

catalysis. The Rh coordination sphere and zeolite framework are highlighted in red and blue, respectively. The confinement effect, exerted on the microenvironment between the Rh coordination sphere and zeolite framework, is illustrated by the green radio-wave symbol.

enabled the visualization of isolated Rh atoms that were confined within the ten-membered-ring channels of the MEL zeolite.

Fourier transform infrared (FT-IR) spectroscopy was then used to examine the configuration of Rh species before and after the oxidative disruption treatments. For the **0.17Rh@MEL**, the chemisorption of CO on Rh led to the appearance of three distinct infrared bands (Fig. 2h). The band centred at $2,050\text{ cm}^{-1}$ was ascribed to linearly bound CO on the Rh clusters^{14,15}, whereas the other two bands at $2,082$ and $2,006\text{ cm}^{-1}$ represented the symmetric and asymmetric modes, respectively, of CO chemisorbed on isolated Rh sites^{11,13}. By contrast, after the oxidative disruption treatment, the infrared signal associated with linear CO adsorption diminished, leaving behind the sole *gem*-dicarbonyl adsorption mode. A plausible explanation was that each Rh site, regardless of being isolated or part of a Rh cluster, preferred the configuration of *gem*-dicarbonyl binding on exposure to the CO environment.

To gain insight into the short-range atomic structure of Rh, we conducted X-ray absorption spectroscopy (XAS) study on both **0.17Rh@MEL** and **0.17Rh_{od}@MEL**. The analysis of the X-ray absorption near edge structure (XANES) (Fig. 2i) revealed that the Rh species in **0.17Rh@MEL** predominantly existed in the form of metallic clusters, as indicated by the similar energy of its absorption edge and white-line intensity with respect to those from reference Rh foil. By fitting the extended X-ray absorption fine structure (EXAFS) spectra (Fig. 2j and Supplementary Figs. 6 and 7), we determined that each Rh atom was averagely coordinated to about 5.6 neighbouring Rh atoms within the first coordination shell (Supplementary Table 3). By contrast, the average oxidation state of each Rh in **0.17Rh_{od}@MEL** was increased, as evidenced by the blueshift of its XANES absorption edge^{14,16} (see Supplementary Fig. 8 and Supplementary Table 4 for details), and each Rh atom was only coordinated by approximately 4.0 neighbouring Rh atoms within the first coordination shell. Our further combined EXAFS, STEM, FT-IR and mathematical analyses led to the conclusion

that roughly 13% of the Rh species in the sample existed as isolated Rh sites and the remaining 87% was in the form of Rh clusters, both comprising surficial Rh(I)-*gem*-dicarbonyl moieties (see details in the ‘Explaining Rh speciation of the samples’ section of Methods). Although some approximations were made and thus uncertainties were introduced, it was still helpful to understand the complexity of Rh speciation, and a set of representative structurally reasonable models were accordingly proposed (Supplementary Fig. 9).

It is known that even a small fraction of Rh species exposed on the external surface of zeolites may make a substantial contribution to the overall catalytic performance^{17,18}. Despite the high efficiency in encapsulation of Rh into the MEL pores, the deposition of a small amount of Rh species on the external surface was still inevitable, which may have a negative impact on the regioselective hydroformylation of propene. On the basis of this rationale, we sought to use large organosulfur molecules to selectively poison the external Rh sites and only allow the hydroformylation reaction to take place within the zeolite channels. Specifically, 2,4-dimethylbenzenethiol (DMBT) was used as the ideal organosulfur molecule because its kinetic diameter (8.1 \AA) exceeded the aperture width of MEL (Fig. 3a) and thus its diffusion into the zeolite channels was probably restricted. Indeed, on exposure to 500 Pa of DMBT/CO mixture at 90°C , the intensity of CO absorbance in **0.17Rh_{od}@MEL** gradually diminished over time (Supplementary Fig. 10), indicating the success of organosulfur poisoning at the external Rh sites.

Subsequently, a series of experiments for the hydroformylation of propene catalysed by **0.17Rh_{od}@MEL** were conducted (Fig. 3b). In the absence of DMBT poisoning, the pristine **0.17Rh_{od}@MEL** exhibited the highest activity with a TOF of about $8,100\text{ h}^{-1}$ but a moderate regioselectivity favouring the formation of *n*-butanal ($n/i = 4.9$). Notably, on the addition of an increasing amount of DMBT, the observed regioselectivity of *n*-butanal substantially increased from an n/i ratio of 20

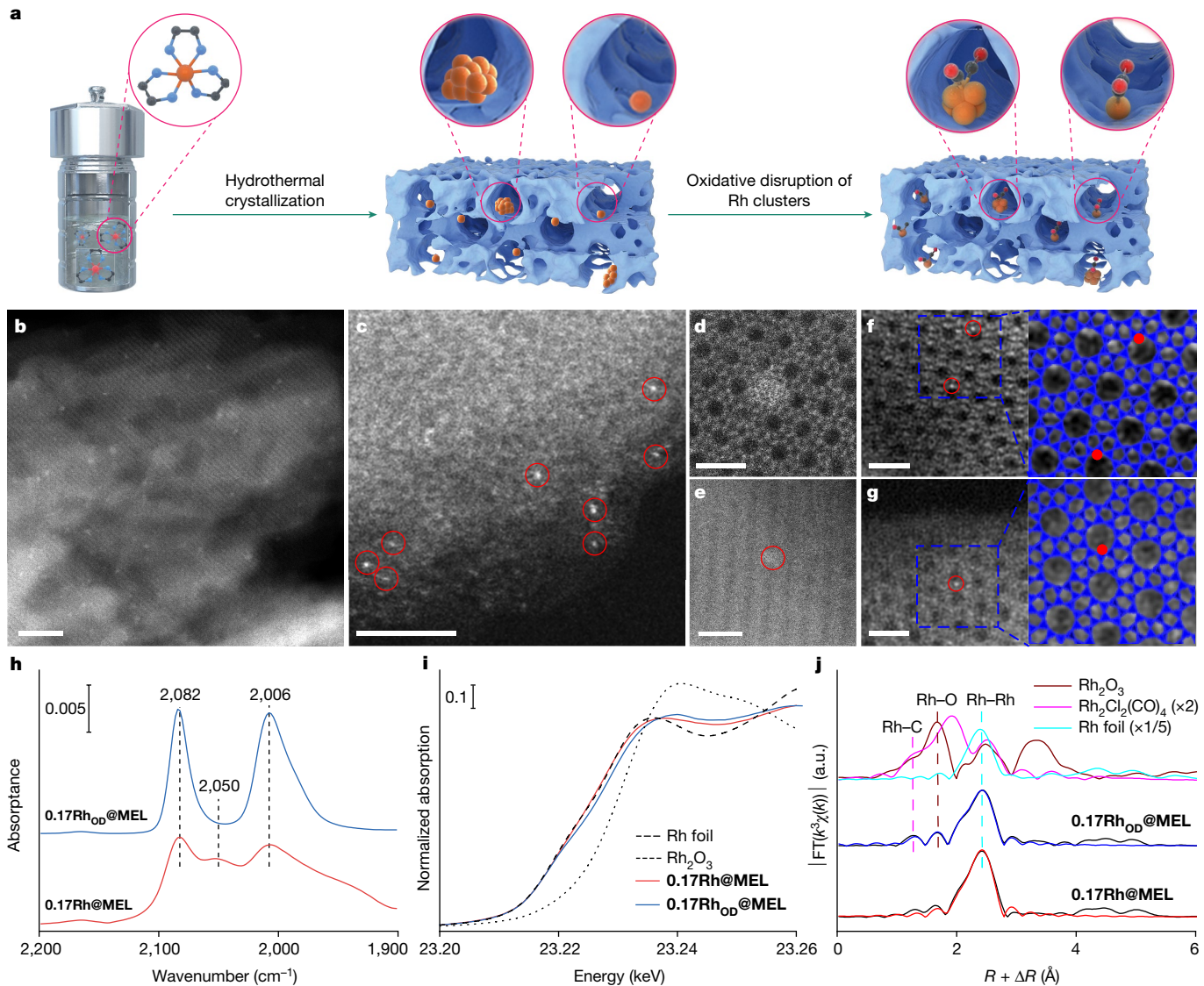


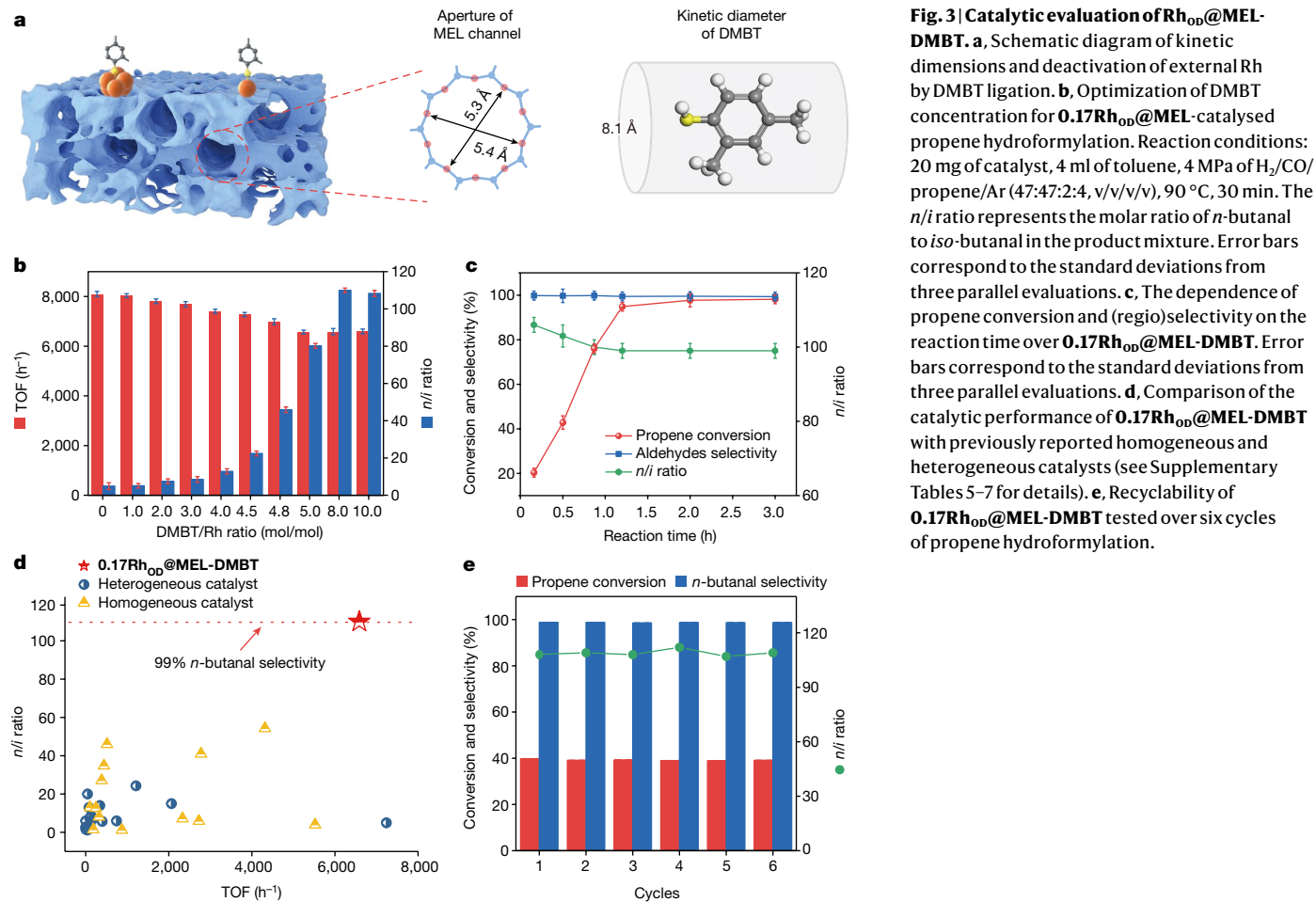
Fig. 2 | Preparation and characterization of Rh@MEL and Rh_{od}@MEL. **a**, Synthetic scheme of Rh_{od}@MEL. **b–g**, Aberration-corrected ADF-STEM images of 0.17Rh_{od}@MEL. Isolated Rh atoms are identified in the image of a thin edge of sample, as marked by red circles in **c**. Rh clusters are immobilized within the zeolite channels, as depicted in **d** and **e**. **f,g**, The locations of the isolated Rh atoms, as indicated by red dots, are visualized by superimposing

zeolite framework onto magnified area of images taken along <100>. Scale bars, 10 nm (**b**), 2 nm (**c–g**). **h**, FT-IR spectra of CO chemisorption on 0.17Rh@MEL and 0.17Rh_{od}@MEL. Normalized XANES (**i**) and FT-EXAFS (**j**) spectra with curve-fitting at the Rh K-edges of 0.17Rh@MEL and 0.17Rh_{od}@MEL. a.u., arbitrary units.

to 80 within a narrow range of DMBT/Rh ratio from 4.5 to 5.0. Such a trend continued until the DMBT/Rh ratio was 8.0. The resulting catalyst, namely, 0.17Rh_{od}@MEL-DMBT, achieved unprecedented high regioselectivity (*n/i* > 110) and chemoselectivity to butanal (>99%) from the hydroformylation of propene (Supplementary Fig. 11). Further addition of DMBT beyond 8.0 equivalents did not lead to noticeable changes in either chemoselectivity or regioselectivity. More importantly, the activity of all DMBT-poisoned catalysts remained very high, with TOF values above 6,500 h⁻¹. It was worth noting that the above-described TOF calculation reflected an average activity for different Rh sites and thus underestimated the activity of the most active species. Of our effort in the optimization of the catalytic performance (Supplementary Figs. 12 and 13), although the *n/i* ratio seemed to clearly decline in the exploited pressure range 0.5–4.0 MPa, when converted into the regioselectivity of *n*-butanal, it was indeed entirely above 99%, reflecting its small variance as a function of the applied pressure. Such a trend was not beyond our expectation and was also consistent with the literature^{19,20}. Both

the *n/i* ratio and overall aldehydes selectivity showed slight decreases along with the reaction process but still remained very high when propene was completely converted (Fig. 3c). Collectively, it was evident that our 0.17Rh_{od}@MEL-DMBT showed excellent regioselectivity and activity, surpassing all previously reported heterogeneous and most homogeneous catalysts in the hydroformylation of propene (Fig. 3d and Supplementary Tables 5–7). Besides, the superior catalytic stability of 0.17Rh_{od}@MEL-DMBT was also witnessed in the recycling and continuous flow experiment (Fig. 3e and Supplementary Figs. 14 and 15).

As well as 0.17Rh_{od}@MEL, two more samples with a Rh mass loading of 0.05 wt% and 0.33 wt% were also prepared for catalytic studies (Supplementary Figs. 16–18 and Supplementary Table 2). The Rh species in both samples remained in the form of either isolated [Rh(CO)₂] or ultrafine Rh clusters with exposed [Rh(CO)₂] on the cluster surface, as evidenced by ADF-STEM and FT-IR characterization (Supplementary Fig. 19). These samples were subjected to DMBT poisoning and termed 0.05Rh_{od}@MEL-DMBT and 0.33Rh_{od}@MEL-DMBT, respectively.



All three catalysts exhibited a comparable regioselectivity in the hydroformylation of propene (Supplementary Figs. 20–22), further supporting our predictions on the creation of a unique microenvironment for the encaged Rh species on the organosulfur poisoning of the external Rh sites.

In situ FT-IR spectroscopy was used to gain more mechanistic insights of the propene hydroformylation on $0.17\text{Rh}_{\text{op}}@\text{MEL-DMBT}$ (Fig. 4 and Supplementary Fig. 23). Before exposure to the reaction medium, two observed CO bands centred at 2,082 and 2,006 cm^{-1} could be assigned to the symmetrical and asymmetrical modes for CO chemisorption in $[\text{Rh}(\text{CO})_2]$ ($\text{Rh}^{\text{I}}: d^8, 16 \text{e}^-$ configuration)^{11,13}. On initiation of the catalytic reaction, these bands smoothly shifted over 13 min, revealing two new CO adsorption bands at 2,073 and 1,998 cm^{-1} , tentatively attributed to the symmetrical and asymmetrical stretching modes of $[\text{HRh}(\text{CO})_2]$ ($\text{Rh}^{\text{I}}: d^8, 18 \text{e}^-$ configuration)^{21,22}. It is well documented that heteroatoms (for example, oxygen) bonding to metal centres (Lewis acids) in various metal–support interfaces can serve as conjugate bases capable of accepting protons. In the presence of such a Lewis-acid-bonded pair ('M–O' bond), heterolytic dissociation of H_2 can occur, forming the 'O–H' proton adduct and 'M–H' metal hydride simultaneously^{23,24}. We speculated that a similar scenario may exist in our case, in which the heterolytic dissociation of H_2 across the 'Rh–O' bond at the interfacial zeolite occurred and the resulting H⁺ migrates to the adjacent $[\text{Rh}(\text{CO})_2]$ site to form $[\text{HRh}(\text{CO})_2]$ (refs. 12,22). Another prominent CO band arising at 2,038 cm^{-1} under the reaction conditions was consistent with the expected CO infrared pattern of $[\text{HRh}(\text{CO})]$ ¹¹, which is usually believed to be generated through the dissociation of a CO molecule from the parent $[\text{HRh}(\text{CO})_2]$. In homogeneous Rh-catalysed hydroformylation, $[\text{HRh}(\text{CO})]\text{L}_x$ ($\text{Rh}^{\text{I}}: d^8, 16 \text{e}^-$) has been widely recognized as the catalytically active Rh species²⁵. Likewise, the formation of an active site

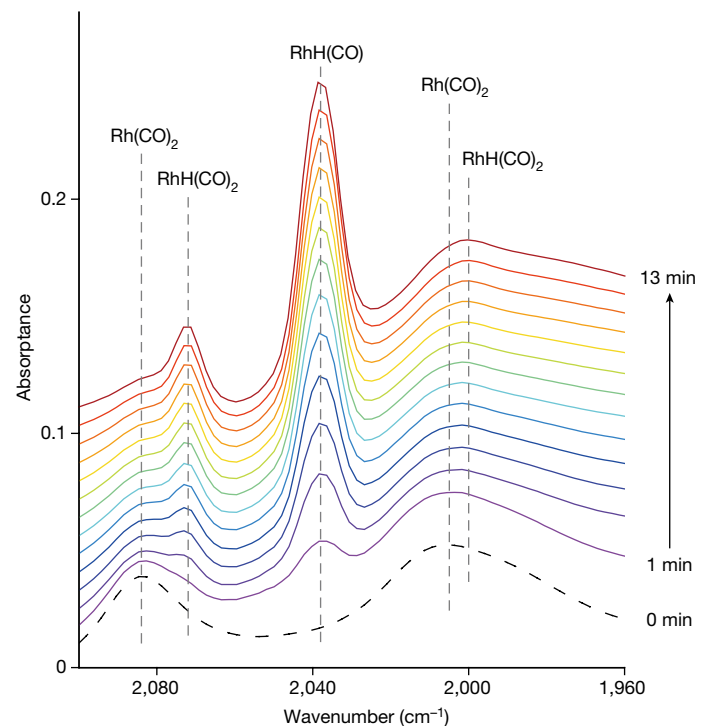


Fig. 4 | In situ FT-IR study. Time-dependent FT-IR spectra in the carbonyl stretching region of $0.17\text{Rh}_{\text{op}}@\text{MEL}$ on exposure to the hydroformylation atmosphere ($\text{H}_2/\text{CO}/\text{propene}/\text{Ar} = 47:47:2:4, \text{v/v/v/v}, 4 \text{ MPa}$) at 90 °C. The gaseous CO signal was subtracted from the original spectra (Supplementary Fig. 23).

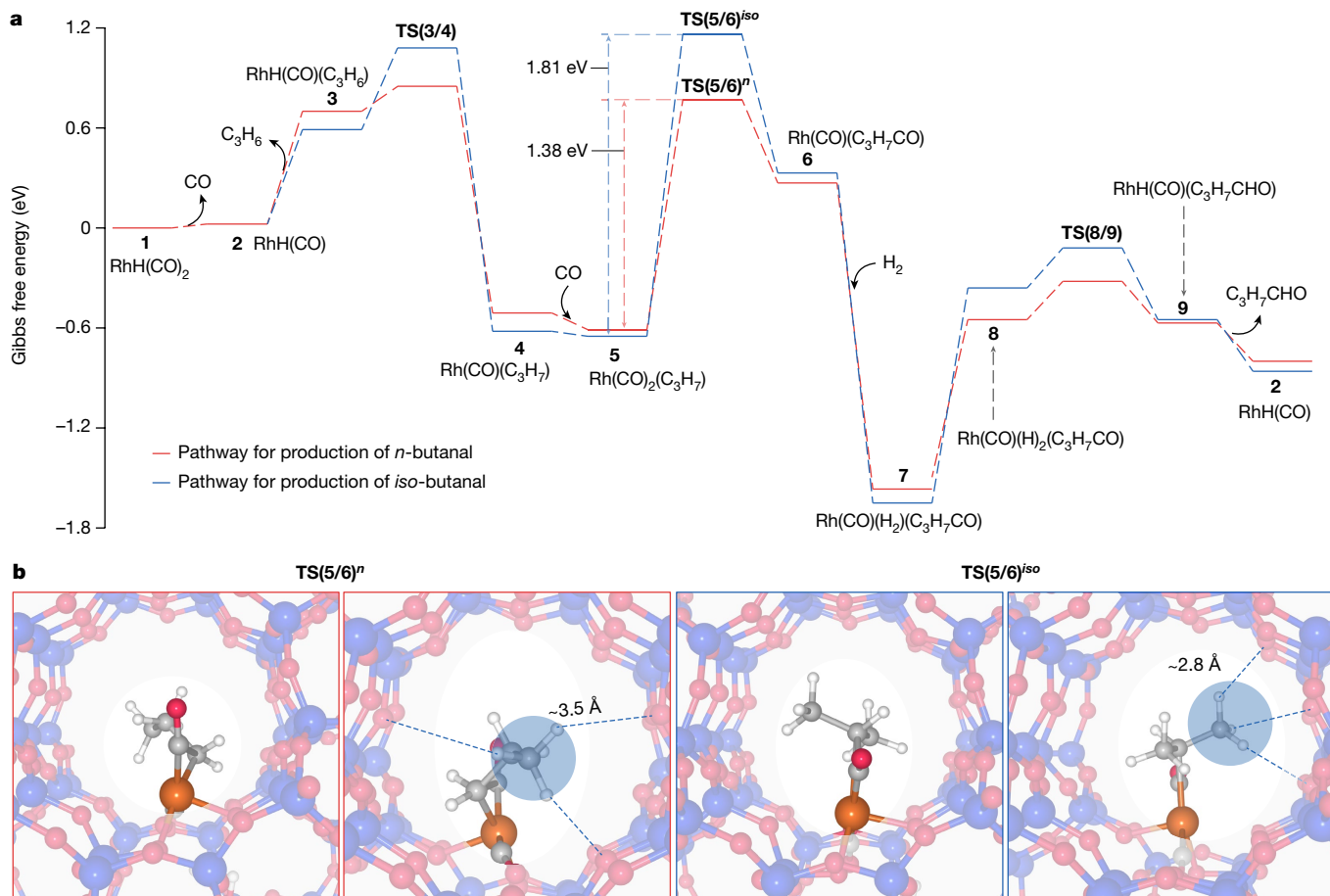


Fig. 5 | Theoretical study of propene hydroformylation on [RhH(CO)₂]@MEL. **a**, Gibbs free energy profiles of propene hydroformylation for the production of *n*-butanal (red) and *iso*-butanal (blue) on the [RhH(CO)₂]@MEL model. The bold numbers correspond to the intermediates in Supplementary Fig. 27, whereas TS represents the transition state. The Gibbs free energies

were calibrated at 90 °C. **b**, Diagram of the transition state for the CO insertion step in two different pathways. **TS(5/6)ⁿ** and **TS(5/6)^{iso}** denote the transition state of the elementary step 5 → 6 in the pathway for the production of *n*-butanal and *iso*-butanal, respectively. The Rh, Si, C, O and H atoms are respectively shown in orange, blue, grey, red and white.

containing HRh(CO)] (Rh¹: d⁸, 16 e⁻) is considered a prerequisite for the initiation of the subsequent heterogeneous cycle²¹. Therefore, we attributed the steadily increasing intensity of the CO band at 2,038 cm⁻¹ to the accumulation of [HRh(CO)] within the measured time window. Further evidence for the existence of the Rh carbonyl species was also obtained from in situ XAS studies (Supplementary Figs. 24 and 25 and Supplementary Table 8), in which the typical signal for positively charged Rh species and relevant coordination structure remained unchanged on exposure to the reaction medium.

To the best of our knowledge, it remains very challenging to experimentally acquire reliable thermodynamic and kinetic data under operating conditions in the zeolite systems as direct evidence to support the imagined shape selectivity and we therefore resorted to the theoretical route to seek the possible rationale. In particular, we performed density functional theory (DFT) calculations to acquire the energy landscape on a theoretical [RhH(CO)₂]@MEL model (Supplementary Figs. 26–28), which represented the isolated Rh active sites within the MEL pores. Overall, the energy profile revealed that the aldehyde production was predominantly governed by the CO insertion step (from [Rh(CO)₂(C₃H₇)] (5) to [Rh(CO)(C₃H₇CO)] (6)), which exhibited the highest energy barrier among all the reaction coordinates (Fig. 5a). The insertion of CO at C¹ in C¹H₂=C²H³H₃ favoured the formation of *n*-butanal, whereas the insertion on C² led to the undesired *iso*-butanal. Therefore, a comparative analysis of the energetics associated with these two competitive CO insertion steps provided insights into the regioselectivity of butanal formation. In both pathways, the CO insertion step proceeded through

a three-centre transition state (**TS(5/6)**), accompanied by elongation of the Rh–propyl bond and migration of the propyl group towards the carbonyl. The elongated Rh–propyl bond pushed the propyl group away from the Rh site, forcing the C³-methyl group to approach the O atoms in the zeolitic lattice. This introduced notable strain into this intermediate species, as evidenced by the considerably increased energy barrier. Notably, the energy barrier for the CO insertion step at C¹ was 0.43 eV lower than that at C², indicating the great potential for the production of *n*-butanal over *iso*-butanal. Also, an apparent orientation of the propyl group along the zeolite channel (*b* axis) was observed in **TS(5/6)ⁿ**, whereas **TS(5/6)^{iso}** exhibited a notable distortion of the methyl tail perpendicular to the *b*-axis direction, resulting in closer contact with the zeolitic framework (Fig. 5b). This was further supported by the greatly reduced distance between the O atoms in the zeolite framework and the H atoms in the C³-methyl group of **TS(5/6)^{iso}** compared with **TS(5/6)ⁿ**. Consequently, it was reasonable to conclude that the *iso*-butanal formation pathway experiences stronger steric hindrance imposed by the zeolite channels compared with the other route leading to *n*-butanal, consistent with the pronounced difference in the energy barriers between these two pathways. It was noted that there was a large difference in the calculated and measured activation energies. Nevertheless, this was not unexpected and did not affect the overall conclusion on the regioselectivity (see more discussion in the ‘Theoretical calculations’ section of Methods). Our parallel calculations performed on the cluster model [Rh₆H(CO)₂]@MEL revealed comparable framework-directing effect in the exclusive formation of

n-butanal (see Supplementary Figs. 29 and 30 for details). By contrast, such an effect was not noticeable for the Rh site located on the exterior of the MEL zeolite (Supplementary Figs. 31–33). These DFT calculation results demonstrated that the confinement effect arising from zeolitic channels played a decisive role in imposing constraints on the reaction intermediates during the hydroformylation of propene, leading to the achieved excellent regioselectivity.

Online content

Any methods, additional references, Nature Portfolio reporting summaries, source data, extended data, supplementary information, acknowledgements, peer review information; details of author contributions and competing interests; and statements of data and code availability are available at <https://doi.org/10.1038/s41586-024-07342-y>.

1. Pospech, J., Fleischer, I., Franke, R., Buchholz, S. & Beller, M. Alternative metals for homogeneous catalyzed hydroformylation reactions. *Angew. Chem. Int. Edn* **52**, 2852–2872 (2013).
2. Arnoldy, P. in *Rhodium Catalyzed Hydroformylation* (Van Leeuwen, P. W. N. M. & Claver, C., 203–231 (Springer, 2000)).
3. Franke, R., Selent, D. & Borner, A. Applied hydroformylation. *Chem. Rev.* **112**, 5675–5732 (2012).
4. Liu, B. et al. Heterogeneous hydroformylation of alkenes by Rh-based catalysts. *Chem* **8**, 2630–2658 (2022).
5. Shylesh, S. et al. In situ formation of Wilkinson-type hydroformylation catalysts: insights into the structure, stability, and kinetics of triphenylphosphine- and xantphos-modified Rh/SiO₂. *ACS Catal.* **3**, 348–357 (2013).
6. Li, C. et al. Single atom dispersed Rh-biphephos&PPh₃@porous organic copolymers: highly efficient catalysts for continuous fixed-bed hydroformylation of propene. *Green Chem.* **18**, 2995–3005 (2016).
7. Riisager, A. et al. Very stable and highly regioselective supported ionic-liquid-phase (SILP) catalysis: continuous-flow fixed-bed hydroformylation of propene. *Angew. Chem. Int. Edn* **44**, 815–819 (2005).
8. Srinivas, G. & Chuang, S. S. C. An *in-situ* infrared study of the formation of *n*- and iso-butraldehyde from propylene hydroformylation on Rh/SiO₂ and sulfided Rh/SiO₂. *J. Catal.* **144**, 131–147 (1993).
9. Smit, B. & Maesen, T. L. Towards a molecular understanding of shape selectivity. *Nature* **451**, 671–678 (2008).
10. Ren, L. et al. Designed copper-amine complex as an efficient template for one-pot synthesis of Cu-SSZ-13 zeolite with excellent activity for selective catalytic reduction of NO_x by NH₃. *Chem. Commun.* **47**, 9789–9791 (2011).
11. McClure, S. M., Lundwall, M. J. & Goodman, D. W. Planar oxide supported rhodium nanoparticles as model catalysts. *Proc. Natl Acad. Sci. USA* **108**, 931–936 (2011).
12. Ro, I. et al. Bifunctional hydroformylation on heterogeneous Rh-WO_x pair site catalysts. *Nature* **609**, 287–292 (2022).
13. Yates, D. J. C., Murrell, L. L. & Prestridge, E. B. Ultradispersed rhodium rafts: their existence and topology. *J. Catal.* **57**, 41–63 (1979).
14. Qi, L. et al. Ethene hydroformylation catalyzed by rhodium dispersed with zinc or cobalt in silanol nests of dealuminated zeolite beta. *J. Am. Chem. Soc.* **145**, 2911–2929 (2023).
15. Matsubu, J. C., Yang, V. N. & Christopher, P. Isolated metal active site concentration and stability control catalytic CO₂ reduction selectivity. *J. Am. Chem. Soc.* **137**, 3076–3084 (2015).
16. Goellner, J. F., Gates, B. C., Vayssilov, G. N. & Rösch, N. Structure and bonding of a site-isolated transition metal complex: rhodium dicarbonyl in highly dealuminated zeolite Y. *J. Am. Chem. Soc.* **122**, 8056–8066 (2000).
17. Choi, M., Wu, Z. & Iglesia, E. Mercaptosilane-assisted synthesis of metal clusters within zeolites and catalytic consequences of encapsulation. *J. Am. Chem. Soc.* **132**, 9129–9137 (2010).
18. Goel, S., Wu, Z., Zones, S. I. & Iglesia, E. Synthesis and catalytic properties of metal clusters encapsulated within small-pore (SOD, GIS, ANA) zeolites. *J. Am. Chem. Soc.* **134**, 17688–17695 (2012).
19. Li, C. et al. Xantphos doped Rh/POPs-PPh₃ catalyst for highly selective long-chain olefins hydroformylation: chemical and DFT insights into Rh location and the roles of Xantphos and PPh₃. *J. Catal.* **353**, 123–132 (2017).
20. Pruitt, R. L. & Smith, J. A. Low-pressure system for producing normal aldehydes by hydroformylation of α -olefins. *J. Org. Chem.* **34**, 327–330 (1969).
21. Zheng, Y. et al. Boosting the hydroformylation activity of a Rh/CeO₂ single-atom catalyst by tuning surface deficiencies. *ACS Catal.* **13**, 7243–7255 (2023).
22. Farpón, M. G. et al. Rhodium single-atom catalyst design through oxide support modulation for selective gas-phase ethylene hydroformylation. *Angew. Chem. Int. Edn* **135**, e202214048 (2022).
23. Aireddy, D. R. & Ding, K. Heterolytic dissociation of H₂ in heterogeneous catalysis. *ACS Catal.* **12**, 4707–4723 (2022).
24. Lu, J., Aydin, C., Browning, N. D. & Gates, B. C. Hydrogen activation and metal hydride formation trigger cluster formation from supported iridium complexes. *J. Am. Chem. Soc.* **134**, 5022–5025 (2012).
25. Torrent, M., Sola, M. & Frenking, G. Theoretical studies of some transition-metal-mediated reactions of industrial and synthetic importance. *Chem. Rev.* **100**, 439–494 (2000).

Publisher's note Springer Nature remains neutral with regard to jurisdictional claims in published maps and institutional affiliations.

Springer Nature or its licensor (e.g. a society or other partner) holds exclusive rights to this article under a publishing agreement with the author(s) or other rightsholder(s); author self-archiving of the accepted manuscript version of this article is solely governed by the terms of such publishing agreement and applicable law.

© The Author(s), under exclusive licence to Springer Nature Limited 2024

Methods

Materials

Tetrabutylammonium hydroxide (40 wt% in H₂O), ethylenediamine (≥99.5%), tetraethyl orthosilicate (≥99.5%), potassium hydroxide (anhydrous, ≥99.95% trace metals basis), Rh(III) chloride hydrate (≥99.9% trace metals basis), ethanol (≥99.5%), toluene (anhydrous, 99.8%), *n*-nonane (99.8%), cyclohexane (≥99.5%) and cyclooctene (≥99.5%) were purchased from Sigma-Aldrich. Fumed silica (surface area of approximately 350–420 m² g⁻¹), 2,4-dimethylthiophenol (>96%) and 1-octene (>99.5%) were obtained from Alfa Aesar. All reagents, unless otherwise specified, were used without further purification. Deionized water (resistivity <18.2 MΩ cm) was obtained from an EMD Millipore Milli-DI Water Purification System. The ultrahigh-purity Ar (99.999%), H₂ (99.999%), CO (99.999%), H₂/Ar mixture (10:90, v/v) and H₂/CO/propene/Ar (47:47:2:4, v/v/v/v) gases were purchased from Praxair. All of the gases were purified by passing through in-line gas purifiers (Big Universal Trap, Agilent) to remove trace amounts of oxygen, water and hydrocarbons.

Synthesis of Rh@MEL materials

The encapsulation of Rh within MEL zeolitic channels has never been reported previously, to our knowledge, and the syntheses of our new Rh@MEL materials were modified from the precedent one-pot hydrothermal crystallization recipe, in which encapsulation of Pt and Rh into the MFI channels was successfully achieved^{26,27}. In the representative synthesis of the **0.17Rh@MEL**, a gel solution was prepared by dissolving 0.030 g of KOH (0.5 mmol) in 2.32 ml of deionized H₂O and then mixing with 3.880 g of tetrabutylammonium hydroxide (6.0 mmol) and 4.120 g of tetraethyl orthosilicate (19.8 mmol). A metal precursor solution was prepared by dissolving 0.0045 g of Rh(III) chloride hydrate (0.017 mmol) and 100 μl of ethylenediamine in 100 μl of deionized H₂O. This metal precursor was added dropwise into the gel solution with vigorous stirring. The gel solution was then hydrolysed at 30 °C for 10 h with stirring (500 r.p.m.). The molar composition of the obtained gel was 66.7 (K₂O):5.282.6 (SiO₂):1.600.8 (TBAOH): 6,8921.1 (H₂O):4.0 (Rh):400.2 (NH₂CH₂CH₂NH₂). The resultant yellow solution was transferred into a 50-ml Teflon-lined stainless autoclave and heated at 130 °C for 24 h under static conditions. Following the hydrothermal crystallization, the solid product was isolated by centrifugation and sequentially washed with deionized water and ethanol. Subsequently, it was dried at 80 °C for 12 h in ambient air. The obtained solid sample was further calcined in static air at 560 °C for 5 h and then reduced under a flow of H₂/Ar mixture at 600 °C for 2 h. The as-prepared sample was denoted **0.17Rh@MEL**.

Synthesis of Rh_{OD}@MEL materials

A CO pretreatment was subsequently conducted to disrupt Rh clusters into isolated atoms and thus generate the atomically dispersed Rh sites on the original **0.17Rh@MEL** sample. For details, the **0.17Rh@MEL** sample was loaded into quartz tubes and subjected to heating under a continuous flow of CO (0.5 MPa) at 90 °C for 2 h. The Rh loading in the resulting **0.17Rh_{OD}@MEL** samples was determined by inductively coupled plasma optical emission spectroscopy (ICP-OES) analysis. The syntheses of **0.05Rh_{OD}@MEL** and **0.33Rh_{OD}@MEL** were succeeded under identical conditions, except using different amounts of Rh(III) chloride hydrate (0.0012 g and 0.0092 g, respectively) within the previously mentioned synthesis procedure.

Material characterization

ICP-OES measurement. The metallic elemental composition of prepared materials was determined by ICP-OES using an Optima 2100 DV spectrometer.

Powder X-ray diffraction measurement. Powder X-ray diffraction patterns were collected at room temperature using a Bruker D8 ADVANCE

powder diffractometer with a Cu K α radiation source ($\lambda = 1.5406 \text{ \AA}$) operating at 40 kV and 40 mA. The data were obtained by a step-scan mode over a 2θ range from 5° to 90°, with a scanning step of 0.02°. Calibration of 2θ was accomplished using LaB₆ powder.

ADF-STEM measurement. The ADF-STEM images were collected at 300 kV with aberration-corrected STEM (FEI, Titan Cubed Thermis G2 and JEOL, JEM-ARM300F). For all data, either 2,048 × 2,048-pixel or 1,024 × 1,024-pixel images were recorded and the dwell time for each pixel was varied from 3 μs up to 12 μs . The beam current used was below 10 pA. The mapping of energy-dispersive spectroscopy was performed using TEM (FEI, Talos) operated at 200 kV.

FT-IR spectroscopy. FT-IR measurements were performed using a Bruker VERTEX 70v spectrometer equipped with a mercury cadmium telluride detector. The spectra were recorded in transmission mode using averaging 64 scans at a resolution of 4 cm⁻¹ within the range 1,000–4,000 cm⁻¹. Approximately 20 mg of samples were pressed into a self-supported wafer with a diameter of 13 mm and loaded into a specially designed high-temperature infrared cell fitted with a BaF₂ window and connected to a vacuum-adsorption apparatus, which allows for dynamic pressure control (Supplementary Fig. 34). Before the adsorption measurement, the samples were reduced under a flow of atmospheric H₂ at 500 °C for 1 h and then evacuated for 30 min, followed by cooling down to 25 °C under dynamic vacuum. Afterwards, CO was admitted into the cell with stepwise pressure of CO and the infrared spectra were continuously recorded until the signal stabilized. To monitor the thiol poisoning process, the evolution of infrared spectra was collected while exposing the oxidatively disrupted samples to a vapour of DMBT carried with CO at 5 mbar. For in situ FT-IR measurements, the oxidatively disrupted samples were loaded into a custom-made infrared cell (Supplementary Fig. 35) with a narrow optical path (200 μm) and then exposed to a mixture of H₂/CO/propene/Ar (47:47:2:4, v/v/v/v) at 90 °C with a total pressure of 4 MPa. The signal of gaseous CO was subtracted from the original FT-IR spectra based on a previously reported data-processing approach²⁸, to eliminate its interference in the observation of the CO signal from Rh carbonyl.

XAS measurement. The XAS study at the Rh K-edge was carried out at the BL14W1 and BL13SSW beamlines of the Shanghai Synchrotron Radiation Facility, using a Si(311) double-crystal monochromator. Data were recorded in fluorescence yield mode, using a four-element Ge detector. Energy calibration was achieved using Rh foil and the tabulated edge energy was defined as the first inflection point in the derivative spectrum. Data reduction and analysis were performed using the ATHENA and ARTEMIS software²⁹. The data were fitted in R-space with theoretical models constructed from FEFF based on the crystal structures of Rh metal and DFT-optimized [Rh(CO)₂]@MEL and [RhH(CO)₂]@MEL. For the XAS measurement, the sample was compressed into flakes of thickness 5 mm and loaded into custom-made cells, followed by pre-treatment under continuous flow of H₂ at 500 °C for 1 h and cooling to 90 °C in an Ar atmosphere. The gas flow was subsequently switched to CO, during which the XAS spectra were recorded to monitor the structural evolution during the oxidative disruption of Rh species. A similar pre-treatment procedure was also adopted before in situ XAS measurement, which was then performed after exposure to pressurized gas of H₂/CO/propene/Ar (4 MPa, 47:47:2:4, v/v/v/v) at 90 °C.

Explaining Rh speciation of the samples

A library containing varieties of models as a statistical foundation for the extraction of Rh–Rh, Rh–O and Rh–C scattering paths was first established. In particular, the Rh–Rh scattering path was extracted from the crystal structure of Rh metal and Rh₆(CO)₁₆. Rh metal is the most commonly used standard and Rh₆(CO)₁₆ is a thermodynamically stable

Article

organometallic compound with Rh cluster size comparable with our case. The Rh–O scattering path was extracted from the crystal structure of Rh_2O_3 and a theoretical $[\text{Rh}(\text{CO})_2]@\text{MEL}$ model optimized from DFT calculations. Rh_2O_3 is the most frequently used Rh oxide standard. The $[\text{Rh}(\text{CO})_2]@\text{MEL}$ model with direct Rh–O bonding to zeolite should be more representative of the catalyst. Extraction of the Rh–C scattering path was based on more known models, $\text{Rh}_2\text{Cl}_2(\text{CO})_4$, $\text{Rh}_4(\text{CO})_{12}$, $\text{Rh}_6(\text{CO})_{16}$ and the theoretical $[\text{Rh}(\text{CO})_2]@\text{MEL}$ model, which all have the same $[\text{Rh}(\text{CO})_2]$ structural unit in common.

All of these extracted Rh–Rh, Rh–C and Rh–O scattering paths together formed 16 combinations available for fitting the Fourier-transformed EXAFS (FT-EXAFS) spectrum of the **0.17Rh_{od}@MEL** catalyst. The fitting was processed in the ARTEMIS software and a good fit should have a small R-factor, which is a measure of the percentage misfit between the data and theory. Through systematic analysis of the fitting results, there was almost no difference in the obtained R-factor following fitting with different combinations (Supplementary Fig. 6).

Meanwhile, to solidify a link between the experimental and theoretical results, we thus chose the crystal structure of Rh metal to extract the Rh–Rh scattering path and the models optimized by DFT calculations to extract the Rh–O and Rh–C scattering paths for fitting with the FT-EXAFS spectrum of **0.17Rh_{od}@MEL** catalyst. The generated theoretical FT-EXAFS spectrum through data fitting and three experimentally obtained FT-EXAFS spectra of reference materials (Rh foil, Rh_2O_3 and $\text{Rh}_2\text{Cl}_2(\text{CO})_4$) are shown in Fig. 2j.

In short, $\text{CN}_{\text{Rh}-\text{Rh}}$ of 4.0, $\text{CN}_{\text{Rh}-\text{O}}$ of 1.0 and $\text{CN}_{\text{Rh}-\text{C}}$ of 1.1 were successfully determined by using the previously established method. This result is clearly indicative of the average number of Rh, O and C atoms that coordinate to each Rh atom in the **0.17Rh_{od}@MEL** through Rh–Rh, Rh–O and Rh–C covalent bonds, and it is statistically meaningful and of high relevance. By comparing the infrared characterization results of isolated Rh sites with a large amount of literature^{11,13,27,30}, the presence of a Rh(I)-*gem*-dicarbonyl structural unit within the isolated sites has been unambiguously confirmed. An important background here is that Rh(I) (d^8 configuration, 16 e^-) ions are well known in classical coordination chemistry for the violation of the 18 e^- rule and they generally adopt a square-planar geometry. It is thus reasonable to infer that the Rh atom in the isolated sites is coordinated with two CO ligands and the other two O atoms from the surface of the internal zeolite channels through Rh–O bonding (Supplementary Fig. 9). In other words, no other Rh atoms are through to coordinate with that from the isolated site. The $\text{CN}_{\text{Rh}-\text{Rh}}$ of the isolated Rh site is therefore assumed to be zero.

Clearly, from a statistical perspective, the experimentally obtained $\text{CN}_{\text{Rh}-\text{Rh},\text{experiment}}$ of 4.0 is the weighted average of those from the $\text{CN}_{\text{Rh}-\text{Rh},\text{isolated site}}$ and $\text{CN}_{\text{Rh}-\text{Rh},\text{cluster}}$ if the isolated sites and the clusters are treated as a whole, respectively. Here, if we can confirm the value of $\text{CN}_{\text{Rh}-\text{Rh},\text{cluster}}$, we should be able to mathematically derive the proportion of isolated sites and clusters in the sample, which will be very helpful for us to understand the impact of introducing complexity from a quantitative perspective.

For Rh atoms in a cluster, the surface Rh atoms are usually unsaturated in coordination and their $\text{CN}_{\text{Rh}-\text{Rh}}$ value is small, whereas the internal Rh atoms are usually coordinated with more neighbour Rh atoms and their $\text{CN}_{\text{Rh}-\text{Rh}}$ value is larger. Therefore, the CN value presented for a cluster (namely, $\text{CN}_{\text{Rh}-\text{Rh},\text{cluster}}$) is also the result of a weighted average of the $\text{CN}_{\text{Rh}-\text{Rh}}$ values of all Rh atoms contained in the cluster.

However, the real situation is that the sample contains Rh clusters of more than one size. As far as we know, there is no effective method so far that can identify the precise proportion of clusters of each size in similar situations. Therefore, we made an approximation here that a cluster with a statistically average size of 0.64 nm, confirmed by the STEM investigation (Supplementary Fig. 3), is used to represent all clusters for subsequent analysis and discussion. Because the size of the cluster is known, according to the method established in the literature³¹,

we can approximately estimate the total number of Rh atoms (N_{atom}) by assuming that the cluster follows a quasi-spherical structure:

$$N_{\text{atom}} = (1.82R/D)^3 \quad (1)$$

in which D is the distance between two adjacent Rh atoms ($D = 2.7\text{ \AA}$) and R is the radius of Rh cluster ($R = 3.2\text{ \AA}$). According to the calculation based on equation (1), we can conclude that a Rh cluster with a size of 0.64 nm has a total of approximately ten Rh atoms.

Moreover, the average number of neighbours for each coordination shell as a function of the number of atoms present in a cluster can be modelled by using a hyperbolic function with four parameters, as documented in the literature³². We thereafter performed calculation of the $\text{CN}_{\text{Rh}-\text{Rh},\text{cluster}}$ using the following equation:

$$\text{CN}_{\text{Rh}-\text{Rh},\text{cluster}} = aN_{\text{atom}}/(b + N_{\text{atom}}) + cN_{\text{atom}}/(d + N_{\text{atom}}) \quad (2)$$

in which a (8.981), b (9.640), c (3.026) and d (1,462.61) are constant parameters taken from the above reference. According to the calculation of equation (2), we can conclude that, in a cluster of ten Rh atoms, each Rh atom is coordinated by approximately 4.6 Rh atoms on average.

With this information in hand, we were able to revisit the previous question of how to mathematically derive the proportion of isolated sites and clusters in the sample, because the experimentally obtained $\text{CN}_{\text{Rh}-\text{Rh},\text{experiment}}$ is the weighted average of those from the $\text{CN}_{\text{Rh}-\text{Rh},\text{isolated site}}$ and $\text{CN}_{\text{Rh}-\text{Rh},\text{cluster}}$. Here, the proportion of the total number of Rh atoms counted for all isolated sites, equivalent to the number of isolated sites, to the total number of Rh atoms of the entire sample was assumed to be x and that of the Rh clusters was presumed to be $(1-x)$ accordingly. Hence, an x value of 0.13 could be determined from equation (3) as follows:

$$\text{CN}_{\text{Rh}-\text{Rh},\text{experiment}} = x\text{CN}_{\text{Rh}-\text{Rh},\text{isolated site}} + (1-x)\text{CN}_{\text{Rh}-\text{Rh},\text{cluster}} \quad (3)$$

This result revealed that roughly 13% of the Rh species in the sample existed as isolated sites and the remaining 87% was in the form of Rh clusters.

Likewise, the experimentally obtained $\text{CN}_{\text{Rh}-\text{O},\text{experiment}}$ (1.0) could be treated as the weighted average of those from the $\text{CN}_{\text{Rh}-\text{O},\text{isolated site}}$ and $\text{CN}_{\text{Rh}-\text{O},\text{cluster}}$, respectively. As the Rh atom is coordinated to two oxygen atoms, the $\text{CN}_{\text{Rh}-\text{O},\text{isolated site}}$ was assumed to be 2. Hence, we were able to obtain the value of $\text{CN}_{\text{Rh}-\text{O},\text{cluster}}$ as 0.9 from equation (4) as follows:

$$\text{CN}_{\text{Rh}-\text{O},\text{experiment}} = 0.13\text{CN}_{\text{Rh}-\text{O},\text{isolated site}} + 0.87\text{CN}_{\text{Rh}-\text{O},\text{cluster}} \quad (4)$$

Similarly, the value of $\text{CN}_{\text{Rh}-\text{C},\text{cluster}}$ could be determined as 1.0 from equation (5) as follows:

$$\text{CN}_{\text{Rh}-\text{C},\text{experiment}} = 0.13\text{CN}_{\text{Rh}-\text{C},\text{isolated site}} + 0.87\text{CN}_{\text{Rh}-\text{C},\text{cluster}} \quad (5)$$

We were keen to obtain the $\text{CN}_{\text{Rh}-\text{O},\text{cluster}}$ of 0.9 and $\text{CN}_{\text{Rh}-\text{C},\text{cluster}}$ of 1.0, as it implies that about an equal number of Rh–C and Rh–O bonds formed in the Rh_{10} cluster. A possible rationale here is that about half of the Rh atoms in the Rh_{10} cluster are bonded to the oxygen atoms of the zeolitic framework and another half of the Rh atoms are bonded to the CO by means of the Rh-*gem*-dicarbonyl configuration. This coordination mode adopted by the Rh_{10} cluster does not conflict with the knowledge we obtained by conducting FT-IR studies on **0.17Rh_{od}@MEL**, only the characteristic infrared feature associating with Rh(I)-*gem*-dicarbonyl witnessed, which proved the rationality of our speculation from another aspect. As such, the representative Rh_6 cluster model proposed in Supplementary Fig. 9 is reasonable, under the premise of making some assumptions in advance.

It was worth noting that the premise of these discussions was based on some assumptions, which would thus bring some deviations. Indeed,

rarely precedent, to the best of our knowledge, has used such a procedure to roughly quantify the component of a complex composition through the interpretation of the fitted results of EXAFS data³³. As such, we prefer not to overinterpret these results but rather take it as a rough reference to illustrate the complexity of Rh species.

The Rh species in the sample, despite being in the form of isolated sites or Rh clusters, were both responsible for the regioselective catalysis owing to comprising superficial Rh(I)-*gem*-dicarbonyl moieties. Besides the isolated Rh sites, the surface Rh atoms of the clusters exposed inside the zeolite pore also adopted the configuration of Rh(I)-*gem*-dicarbonyl, which was proved to be catalytically active in the regioselective hydroformylation of propene. As such, as well as those isolated Rh sites (roughly 13% of the total Rh species), the Rh cluster (about 87% of the total Rh species) surface exposed in the pores can also provide a large number of single-atom Rh sites to promote the reaction and contribute to the resulting regioselectivity.

Evaluating the encapsulation efficiency of Rh@MEL samples

The spatial distribution of Rh species within Rh@MEL samples was determined using the methods proposed in refs. 18,34. In general, the active sites both inside and outside the zeolite channels/voids would contribute to the catalytic conversion of substrates, as long as the diffusion diameter is lower than that of zeolite apertures. By contrast, the molecules that possess larger size than that of zeolite apertures could not access the active sites within the zeolite channels/voids, therefore the contribution to its conversion should be attributed to the metallic species outside the zeolite channels/voids. As such, the proportion of active sites inside the zeolite channels/voids could be estimated on the basis of the difference in the reaction rate between small and large molecules. In particular, we chose 1-octene (kinetic diameter = 5.3 Å) and cyclooctene (kinetic diameter = 8.0 Å) as probe reactants and taking hydrogenation of them as the model reaction to differentiate the relative content of Rh species located outside and inside the channel/voids of MEL zeolite (aperture dimensions 5.3 × 5.4 Å). In detail, the hydrogenation rates for 1-octene and cyclooctene on an unconstrained cluster dispersed on fumed silica (Rh/SiO₂, prepared by wet impregnation) were first measured and the ratio of TOF_{1-octene} and TOF_{cyclooctene} ($\chi_{\text{SiO}_2} = \text{TOF}_{1\text{-octene}}/\text{TOF}_{\text{cyclooctene}}$) was approximately regarded as the standard relative reactivity of these two molecules. Similarly, the χ_{MEL} was also calculated by measuring the ratio of TOF_{1-octene} and TOF_{cyclooctene} on Rh-MEL samples. The proportion of MEL-encapsulated sites was thus estimated as $1 - \chi_{\text{SiO}_2}/\chi_{\text{MEL}}$.

In a typical measurement, Rh@MEL sample, 1-octene (or cyclooctene) and cyclohexane was loaded into the autoclave, which was purged with hydrogen four times and then pressurized to 4 MPa. The autoclave was then heated to 70 °C with stirring at 800 r.p.m. for 20 min and subsequently cooled in an ice bath. The resulting reaction mixture was separated by centrifugation and then mixed with 100 µl of *n*-nonane (internal standard). The mixture was then analysed by an Agilent 8890 gas chromatograph equipped with an HP-5 capillary column (30 m × 0.25 mm × 0.25 µm) and a flame-ionized detector (FID). The TOFs were calculated as the number of molecules converted per hour normalized by the total number of Rh atoms within the samples. To exclude the influence of mass transfer on the reaction rate, the reaction was conducted in the kinetic regime by maintaining the conversion of 1-octene or cyclooctene below 10%.

Catalytic evaluations

The hydroformylation of propene was performed in a 25-mL stainless-steel autoclave with an inner diameter of 28 mm and a height of 42 mm, equipped with an electric heating furnace. In a typical evaluation process, 20 mg of Rh_{on}@MEL sample together with 4 mL of toluene and a certain amount of DMBT were charged in the autoclave, which was then purged with feed gas (H₂/CO/propene/Ar mixture, 47:47:2:4, v/v/v/v) four times and pressurized to 4 MPa. The reaction was conducted

at 90 °C with stirring at 800 r.p.m. for 3 h. Subsequently, the autoclave was cooled to room temperature and carefully depressurized to atmospheric pressure. Then, 100 µl of *n*-nonane was added as an internal standard into the reaction mixture, followed by centrifugation at 10,000 r.p.m. for 5 min to collect the liquid phase of the reaction mixture, which was subsequently analysed by an Agilent 8890 gas chromatograph equipped with an HP-5 capillary column (30 m × 0.25 mm × 0.25 µm) and a FID. The tail gas was collected and analysed by Agilent 8890 gas chromatograph equipped with a thermal conductivity detector and a FID. The permanent gases (Ar, CO and H₂) and hydrocarbons (propene, propane) in the tail gas were separated by an HP-5MS (30 m × 0.25 mm × 0.25 µm) and a GasPro (30 m × 0.32 mm × 0.32 µm) capillary column, respectively. Propene conversion was determined by tracking its concentration changes in both the gaseous and the liquid mixtures, using Ar and *n*-nonane as internal references, respectively. Specifically, the concentration of propene in the liquid mixture was ascertained through ¹H NMR analysis. The catalytic evaluation was also carried out in a stainless-steel fixed-bed reactor with an inner diameter of 9.0 mm. Generally, 0.2 g of 0.17Rh_{on}@MEL catalyst with 60–80 mesh was loaded in the isothermal region of the reactor and pressurized with a gaseous mixture of H₂/CO/propene/Ar (47:47:2:4, v/v/v/v) to 4 MPa, followed by heating to 90 °C with a ramping rate of 1 °C min⁻¹. Then, the liquid mixture of DMBT/toluene (0.72 mmol L⁻¹ of DMBT in toluene) was pumped into the reactor by means of a constant-flux pump. The tail gas was passed through a cold trap to collect the liquid mixture, whereas the volatile gas was analysed by online Agilent 8890 gas chromatography.

The TOF was calculated as the number of aldehydes produced per hour, normalized to the total number of Rh atoms within the samples, as follows:

$$\text{TOF} = \frac{\text{Moles of aldehydes}}{\text{Moles of Rh in the catalyst} \times (1 - \chi_{\text{SiO}_2}/\chi_{\text{MEL}}) \times \text{reaction time}}$$

whereas the $(1 - \chi_{\text{SiO}_2}/\chi_{\text{MEL}})$ represents the proportion of Rh inside the channels/voids with respect to the total Rh loading into the materials. All of the experiments for the estimation of TOFs were conducted with propene conversion below 40%, at which the reaction was assumed to follow a zero-order kinetics (Supplementary Fig. 36). The influence of gas–liquid mass transfer during the catalytic evaluation was minimized, as evidenced by Supplementary Fig. 37. Three replicates for each catalytic run were conducted under identical procedures, with accompanying error bars to reflect the repeatability of the data.

The catalytic recyclability of prepared catalysts was evaluated by recycling the spent samples recovered at the end of each run and used for the next cycle. In detail, the spent catalyst was separated from the reaction mixture by centrifugation and washed with toluene three times, followed by calcination in static air at 560 °C for 5 h and then reduction by H₂/Ar mixture at 500 °C for 1 h.

Theoretical calculations

Periodic DFT calculations were carried out using the Vienna Ab initio Simulation Package (VASP)^{35,36}. The exchange correlation term was described by the generalized gradient approximation using the Perdew–Burke–Ernzerhof functional³⁷ and corrected by Grimme's D3(BJ) dispersion^{38,39}. Valence–core interactions were described by projector-augmented-wave pseudopotentials⁴⁰. Plane-wave expansions with kinetic energies up to 400 eV were chosen as the basis set for all geometry-optimization calculations⁴¹. Both atomic positions and cell dimensions were optimized using a conjugate gradient algorithm until all Hellmann–Feynman forces were less than 0.02 eV Å⁻¹ (refs. 42,43). The partial occupancies of orbitals were determined with the first-order Methfessel–Paxton scheme, in which the smearing width of 0.2 eV was used⁴⁴. The gamma-point mesh was adopted for Brillouin-zone sampling for all cases. The search of transition states was conducted using

Article

the improved dimer^{45,46} and climbing image nudged elastic band^{47,48} methods. All of the calculated Gibbs free energies were corrected at the reaction temperature of 90 °C according to a literature method⁴⁹. It should be noted that, despite taking these adjustments into account, a large deviation from theoretically calculated results and corresponding experimental values has still emerged. Indeed, such a deviation has been broadly witnessed in Rh-catalysed hydroformylation of propene^{21,50}. Inherent computational limitations and approximations usually contributed to the observations^{51,52}. Nonetheless, both the applied theoretical model and the computational method in our calculations were maintained the same throughout the exploration of both reaction pathways. Hence, the above-mentioned deviation between experimental and theoretical results would not affect the overall conclusion. We thus reasoned that the evaluation of the kinetic differences between two reaction pathways by directly comparing their energy barriers under the same benchmark was reliable. Our DFT calculations were carried out only at 4 MPa, which was same as the pressure chosen for the experimental studies, and we reasoned that such an option was appropriate. Moreover, because the change of pressure did not have a large impact on the selectivity (Supplementary Fig. 12), we assumed that it might not be necessary to conduct exhaustive DFT calculations at all other different pressures at the expense of valuable computing resources.

The theoretical model of [Rh(CO)₂]@MEL was constructed by locating the Rh atom within a silanol nest inside the channels of MEL zeolite. In detail, the MEL model was first obtained by structural optimization of a crystalline unit cell of MEL zeolite derived from the Crystallography Open Database. Subsequently, a silanol nest was created by removing one skeletal Si atom from either inside or outside the MEL channel. A single Rh atom was then located in the silanol group and coordinated with two O atoms to generate an isolated Rh mode. The cluster model [Rh₆H(CO)₂]@MEL was constructed using a similar approach, but in which three Rh atoms were separately coordinated with O in the silanol nests.

The kinetic dimensions of molecules were predicted by Multiwfn wavefunction analysis using the Multiwfn 3.7 program⁵³. The molecular model was first optimized by the Gaussian 16 program package at the level of B3LYP/6-311 G(d, p) (refs. 54–57). The derived wavefunction of molecules was imported into the Multiwfn program to obtain the kinetic dimensions based on electron-density surface analysis⁵⁸.

Data availability

The authors declare that all the data supporting the findings of this study are available within the paper and its Supplementary Information files and are also available from the corresponding author on reasonable request. Source data are provided with this paper.

26. Liu, L. et al. Regioselective generation and reactivity control of subnanometric platinum clusters in zeolites for high-temperature catalysis. *Nat. Mater.* **18**, 866–873 (2019).
27. Sun, Q. et al. Zeolite-encaged single-atom rhodium catalysts: highly-efficient hydrogen generation and shape-selective tandem hydrogenation of nitroarenes. *Angew. Chem. Int. Edn* **58**, 18570–18576 (2019).
28. Kaftan, A. et al. Supported homogeneous catalyst makes its own liquid phase. *J. Catal.* **321**, 32–38 (2015).
29. Ravel, B. & Newville, M. ATHENA, ARTEMIS, HEPHAESTUS: data analysis for X-ray absorption spectroscopy using IFEFFIT. *J. Synchrotron Radiat.* **12**, 537–541 (2005).
30. Rice, C. A., Worley, S. D., Curtis, C. W., Guin, J. A. & Tarrer, A. R. The oxidation state of dispersed Rh on Al₂O₃. *J. Chem. Phys.* **74**, 6487–6497 (1981).
31. Marinkovic, N. S., Sasaki, K. & Adzic, R. R. Determination of single- and multi-component nanoparticle sizes by X-ray absorption spectroscopy. *J. Electrochem. Soc.* **165**, J3222–J3230 (2018).
32. Jentys, A. Estimation of mean size and shape of small metal particles by EXAFS. *Phys. Chem. Chem. Phys.* **1**, 4059–4063 (1999).
33. Cao, L. et al. Atomically dispersed iron hydroxide anchored on Pt for preferential oxidation of CO in H₂. *Nature* **565**, 631–635 (2019).
34. Cho, H. J., Kim, D., Li, J., Su, D. & Xu, B. Zeolite-encapsulated Pt nanoparticles for tandem catalysis. *J. Am. Chem. Soc.* **140**, 13514–13520 (2018).
35. Kresse, G. & Hafner, J. Ab initio molecular dynamics for liquid metals. *Phys. Rev. B* **47**, 558–561 (1993).
36. Kresse, G. & Furthmüller, J. Efficiency of ab-initio total energy calculations for metals and semiconductors using a plane-wave basis set. *Comput. Mater. Sci.* **6**, 15–50 (1996).
37. Perdew, J. P., Burke, K. & Ernzerhof, M. Generalized gradient approximation made simple. *Phys. Rev. Lett.* **77**, 3865–3868 (1996).
38. Grimme, S., Antony, J., Ehrlich, S. & Krieg, H. A consistent and accurate *ab initio* parametrization of density functional dispersion correction (DFT-D) for the 94 elements H–Pu. *J. Chem. Phys.* **132**, 154104–154123 (2010).
39. Grimme, S., Ehrlich, S. & Goerigk, L. Effect of the damping function in dispersion corrected density functional theory. *J. Comp. Chem.* **32**, 1456–1465 (2011).
40. Blochl, P. E. Projector augmented-wave method. *Phys. Rev. B* **50**, 17953–17979 (1994).
41. Kresse, G. From ultrasoft pseudopotentials to the projector augmented-wave method. *Phys. Rev. B* **59**, 1758–1775 (1999).
42. Teter, M. P., Payne, M. C. & Allan, D. C. Solution of Schrödinger's equation for large systems. *Phys. Rev. B* **40**, 12255–12263 (1989).
43. Bylander, D. M., Kleinman, L. & Lee, S. Self-consistent calculations of the energy bands and bonding properties of B₂C₂. *Phys. Rev. B* **42**, 1394–1403 (1990).
44. Methfessel, M. & Paxton, A. T. High-precision sampling for Brillouin-zone integration in metals. *Phys. Rev. B* **40**, 3616–3621 (1989).
45. Henkelman, G. & Jónsson, H. A dimer method for finding saddle points on high dimensional potential surfaces using only first derivatives. *J. Chem. Phys.* **111**, 7010–7022 (1999).
46. Heyden, A., Bell, A. T. & Keil, F. J. Efficient methods for finding transition states in chemical reactions: comparison of improved dimer method and partitioned rational function optimization method. *J. Chem. Phys.* **123**, 224101–224115 (2005).
47. Henkelman, G., Uberuaga, B. P. & Jónsson, H. A climbing image nudged elastic band method for finding saddle points and minimum energy paths. *J. Chem. Phys.* **113**, 9901–9904 (2000).
48. Henkelman, G. & Jónsson, H. Improved tangent estimate in the nudged elastic band method for finding minimum energy paths and saddle points. *J. Chem. Phys.* **113**, 9978–9985 (2000).
49. Szczęsný, Á. et al. Breaking linear scaling relationships with secondary interactions in confined space: A case study of methane oxidation by Fe/ZSM-5 zeolite. *ACS Catal.* **9**, 9276–9284 (2019).
50. Jacobs, I., de Bruin, B. & Reek, J. N. Comparison of the full catalytic cycle of hydroformylation mediated by mono- and bis-ligated triphenylphosphine–rhodium complexes by using DFT calculations. *ChemCatChem* **7**, 1708–1718 (2015).
51. Kozuch, S. & Shaik, S. How to conceptualize catalytic cycles? The energetic span model. *Acc. Chem. Res.* **44**, 101–110 (2011).
52. Farkas, A., Hess, F. & Over, H. Experiment-based kinetic Monte Carlo simulations: CO oxidation over RuO₂(110). *J. Phys. Chem. C* **116**, 581–591 (2012).
53. Lu, T. & Chen, F. Multiwfn: a multifunctional wavefunction analyzer. *J. Comput. Chem.* **33**, 580–592 (2012).
54. Frisch, M. J. et al. Gaussian 16, Revision A.03 (Gaussian, Inc., 2016).
55. Becke, A. D. Density-functional exchange-energy approximation with correct asymptotic behavior. *Phys. Rev.* **38**, 3098–3101 (1988).
56. Lee, C., Yang, W. & Parr, R. G. Development of the Colle-Salvetti correlation-energy formula into a functional of the electron density. *Phys. Rev. B* **37**, 785–789 (1988).
57. Becke, A. D. Density-functional thermochemistry. III. The role of exact exchange. *J. Chem. Phys.* **98**, 5648–5652 (1993).
58. Mehio, N., Dai, S. & Jiang, D. Quantum mechanical basis for kinetic diameters of small gaseous molecules. *J. Phys. Chem. A* **118**, 1150–1154 (2014).

Acknowledgements This work was supported by the National Natural Science Foundation of China (nos. 21972161 and 22172186), Major Science and Technology Project of Ordos City (no. 2022EEDSKJZDX001), Autonomous Research Project of State Key Laboratory of Coal Conversion (no. 2022BWZ009), Inner Mongolia Key Research and Development Program (no. 2023YFHH0009), Institute of Coal Chemistry, Chinese Academy of Sciences and Synfuels China Technology Co., Ltd. We also acknowledge the Shanghai Synchrotron Radiation Facility (SSRF) for providing the facility for XAS measurements and the Centre for High-resolution Electron Microscopy (ChEM) for the TEM tests.

Author contributions Z.C., Y.Y. and H.W. conceived the project and designed the study. X.Zha. and TY. conducted synthesis work, catalytic tests and other characterizations. J.Y. performed the theoretical calculations. H.H., F.S., Y.W. and Q.Z. conducted the structural characterizations. X.S., M.D., W.F., J.W., Y.S., X.Zho., K.W. and Y.L. helped with the data analysis. Z.C. and H.W. wrote the manuscript. All authors discussed the results and commented on the manuscript.

Competing interests The authors declare no competing interests.

Additional information

Supplementary information The online version contains supplementary material available at <https://doi.org/10.1038/s41586-024-07342-y>.

Correspondence and requests for materials should be addressed to Hongliu Wan, Yong Yang or Zhi Cao.

Peer review information *Nature* thanks the anonymous reviewers for their contribution to the peer review of this work.

Reprints and permissions information is available at <http://www.nature.com/reprints>.